ACS OMEGA

http://pubs.acs.org/journal/acsodf

Article

Supported Bimetallic Trimers Fe_2M@NG: Triple-Atom Catalysts for CO_2 Electroreduction

Bing Han, Haihong Meng, and Fengyu Li*

Cite This: *ACS Omega* 2022, 7, 16080−16086

Read Online

ACCESS | Metrics & More | Article Recommendations | Supporting Information

ABSTRACT: Excessive accumulation of carbon dioxide in the atmosphere has become a serious environmental problem due to the increasing consumption of fossil fuels in modern society. Reasonably reducing CO_2 in the atmosphere has become a new research hotspot. Electrocatalytic CO_2 reduction reaction (CO_2RR) offers an appealing strategy to reduce the atmospheric CO_2 concentration and to produce value-added chemicals simultaneously. In this paper, two-dimensional (2D) N-decorated graphene (NG)-supported bimetallic trimers (Fe_2M@NG) were designed as triple-atom catalysts (TACs). Theoretical calculations showed that Fe_2M@NG can effectively activate CO_2, and among the 23 TACs examined, Fe_2Ir@NG not only has a good catalytic activity for CO_2RR (limiting potential is 0.49 V for CH_4 formation) but also limits the competing side reaction of the hydrogen evolution reaction (HER). Our theoretical study not only further extends the triple-atom catalysts, but also opens a new door to boost the sustainable CO_2 conversion.

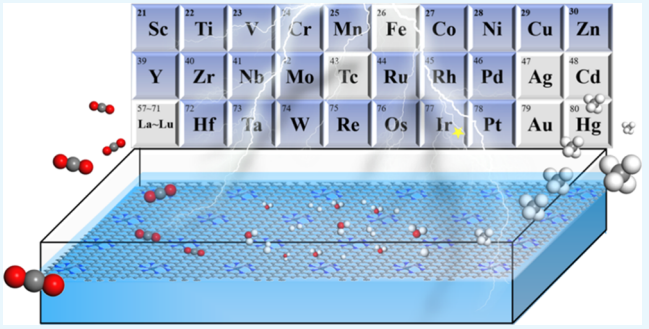

1. INTRODUCTION

For centuries, the utilization of fossil fuels, coal, oil, and natural gas has led to the rapid development of human society.[1−3] However, the ever-increasing energy demands and serious environmental problems require the "optimization" of these traditional energy sources.[4] The massive consumption of these carbonaceous substances results in the continuous increase and accumulation of carbon dioxide (CO_2) in the atmosphere.[5] There are mainly three strategies to prevent increasing atmospheric CO_2 concentration: prohibition of CO_2 release, CO_2 storage, and CO_2 conversion.[6] Among them, the CO_2 conversion technology has attracted the attention as the most promising approach to slow down or even reverse the rising trend of atmospheric carbon dioxide concentration.[7,8] The electrochemical CO_2 reduction reaction (CO_2RR) can directly convert CO_2[9] into high value-added chemicals and fuels,[10,11] and renewable electricity can be used for this electrocatalytic process, resulting in a "net-zero emission" sustainable development.[12] As early as the 1990s, Hori et al. demonstrated the ability of different pure metal catalysts for the electrochemical reduction of CO_2, providing a solid foundation for subsequent CO_2RR.[13] However, CO_2 molecules are chemically inert and the hydrogen evolution reaction (HER) competes fiercely with CO_2RR, and it is challenging to design suitable CO_2RR electrocatalysts with low limiting potential, high current density, high selectivity, and low cost.[14]

Recent studies showed that nitrogen-doped carbon (N-C)-supported transition-metal atom catalysts can effectively reduce CO_2 to single-carbon and multicarbon species.[15−18] N-C-based materials have attracted attention because of their high-temperature resistance, acid and alkali resistance, poison resistance, and environmental protection.[19] Compared to the low activity of pure carbon materials,[20] on the one hand, the N-doped carbon materials as a support can provide stable anchoring sites for the metal atoms and thus endow the system with the characteristics of high stability, selectivity, and low coordination state;[21] on the other hand, its strong interactions with the supported metal atoms can regulate the electronic structure of the catalyst[22] and thus enhance the adsorption of CO_2 and facilitate CO_2RR.[23] The single-atom catalysts (SACs) were considered as the minimum use of metal,[24−27] and expansively, double-atom catalysts (DACs)[27−29] and triple-atom catalysts (TACs)[17,30−33] have gained enormous attention from both theoretical and experimental aspects owing to their synergistic effect and tunable composites in the metal dimers or trimers. For example, the experimentally obtained uniform Ru_3 clusters stabilized by nitrogen species (Ru_3/CN) were found to exhibit excellent catalytic activity for the oxidation of alcohols.[32] Ma and collaborators fabricated Pt_3 clusters on a core−shell nanodiamond@graphene (ND@G) hybrid support,

Received: March 7, 2022
Accepted: April 14, 2022
Published: April 25, 2022

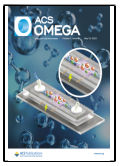

https://doi.org/10.1021/acsomega.2c01385
ACS Omega 2022, 7, 16080−16086

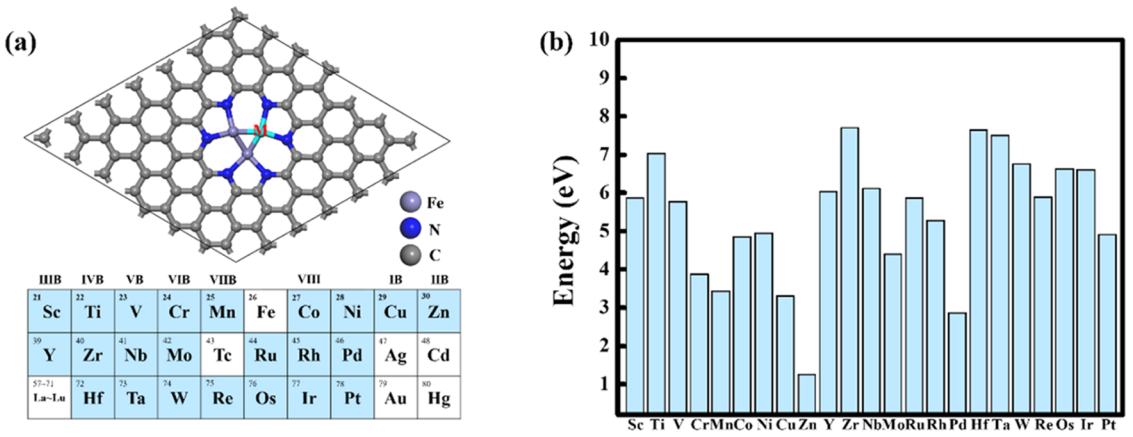

Figure 1. (a) Top view of Fe_2M@NG and the considered transition metal M. (b) Formation energy of Fe_2M@NG.

which inhibits the side reactions and enhances catalytic performance in the direct dehydrogenation of *n*-butane at a low temperature (450 °C) toward olefin products with a selectivity >98%.[33]

Inspired by the theoretical finding that the stable Fe_3@NG (iron trimer-embedded N-decorated graphene) exhibits high catalytic activity to convert CO_2 through the C_2 and C_3 pathways[17] and considering the large space of mediating the combination and electronic coupling of the bimetallic trimers, we explored the stability and catalytic performance of 23 Fe-based bimetallic TACs (Fe_2M@NG) for CO_2 reduction to C_1 products by means of first-principles calculations and elucidated that the Fe_2Ir@NG has excellent catalytic activity for the electroreduction of CO_2 to CH_4 with a small limiting potential of 0.49 V and can also inhibit the competing hydrogen evolution reaction (HER). Our theoretical explorations provide an effective approach for designing bimetallic trimers of high-performance for electrocatalyzing CO_2 reduction.

2. COMPUTATIONAL METHODS

All of the spin-polarized density functional theory (DFT) calculations were carried out using the Vienna *Ab initio* Simulation Package (VASP).[34] The exchange−correlation functional was described by the Perdew−Burke−Ernzerhof (PBE) parameterization of the generalized gradient approximation (GGA).[35] The cutoff energy of 500 eV was adopted. The van der Waals interactions were described using the empirical correction in the Grimme scheme (DFT + D3).[36] The convergence parameters of geometric optimization of the maximum force and energy were designated as 0.01 eV/Å and 10^{-4} eV, respectively. The Brillouin k-point grid was sampled using a 2 × 2 × 1 γ centered Monkhorst−Pack scheme.[37] To weaken the interaction between the layers, a 20 Å vacuum layer was applied. The binding energy (E_b) of Fe_2M@NG based on Fe_2@NG was determined by the following equation

$$E_b = E_{Fe_2@NG} + E_M - E_{Fe_2M@NG}$$

where E_M represents the energy of a single metal atom, $E_{Fe2M@NG}$ and $E_{Fe2@NG}$ are the energies of Fe_2M@NG and Fe_2@NG, respectively. The free energy *G* was calculated based on the hydrogen electrode (CHE) model proposed by Nørskov and colleagues[38]

$$G = E + G(T)$$

where *E* is the reaction energy, which can be directly obtained from the DFT calculation. $G(T) = E_{ZPE} - TS$, where E_{ZPE} and *S* are the zero-point energy and entropy, respectively, which can be obtained by calculating the vibration frequencies.[39] *T* is 298.15 K.[40] The calculated values of gas molecules and intermediates are presented in Tables S1 and S2, respectively. Free energy change (ΔG) of the elementary reaction represents the free energy difference between the product and the reactant ($\Delta G = G_{product} - G_{reactant}$).[41] The limiting potential (η) of the entire reduction process is determined by the potential limiting step, which has the most positive (ΔG_{Max}), as computed by $\eta = \Delta G_{Max}/e$.[42]

3. RESULTS AND DISCUSSION

3.1. Structure and Stability of Fe_2M@NG. A 7 × 7 graphene supercell doped with six N atoms, forming a hole structure similar to that of a pyridine hole, as shown in Figure 1a, was taken as the support for bimetallic trimers.[17] The optimized configurations of the 23 TACs examined are displayed in Figure S1, and the geometric parameters are given in Table S3. The binding energies were in the range of 1.25−7.70 eV (Figure 1b). With similar treatment in ref 17, we performed a first-principles molecular dynamics (FPMD) simulation for Fe_2Zn@NG, whose binding energy is the smallest among the 23 Fe-based TACS, in the NVT ensemble with a temperature of 500 K, a time step of 0.5 fs, and the total time scale of 10 ps. The Fe_2Zn@NG can maintain its original structure through the 10 ps's FPMD simulation at 500 K (Figure S2), indicating the high thermal stability in Fe_2Zn@NG and other bimetallic TACs.

3.2. CO_2 Adsorption. The capture of CO_2 molecules on the catalyst is the first step in the CO_2RR process.[43] Due to the strong interaction between CO_2 and the catalyst, the C−O−C angle of the adsorbed CO_2 in the most stable configuration on these TACs is reduced to 121.36−139.78° compared to 180° of the isolated CO_2 molecule. We denoted the O of CO_2 closer to the TAC as O2, and the other as O1. The lengths of the C−O1 and C−O2 bonds were elongated to 1.20−1.26 and 1.29−1.45 Å, respectively, compared with 1.18 Å of free CO_2. For comparison, C−O1 and C−O2 bonds are 1.21 and 1.33 Å for the adsorbed CO_2 on Fe_3@NG. The adsorption energy (E_{ad}) of CO_2 was estimated by the following formula

$$E_{ad} = E_{*CO_2} - E_* - E_{CO_2}$$

https://doi.org/10.1021/acsomega.2c01385
ACS Omega 2022, 7, 16080−16086

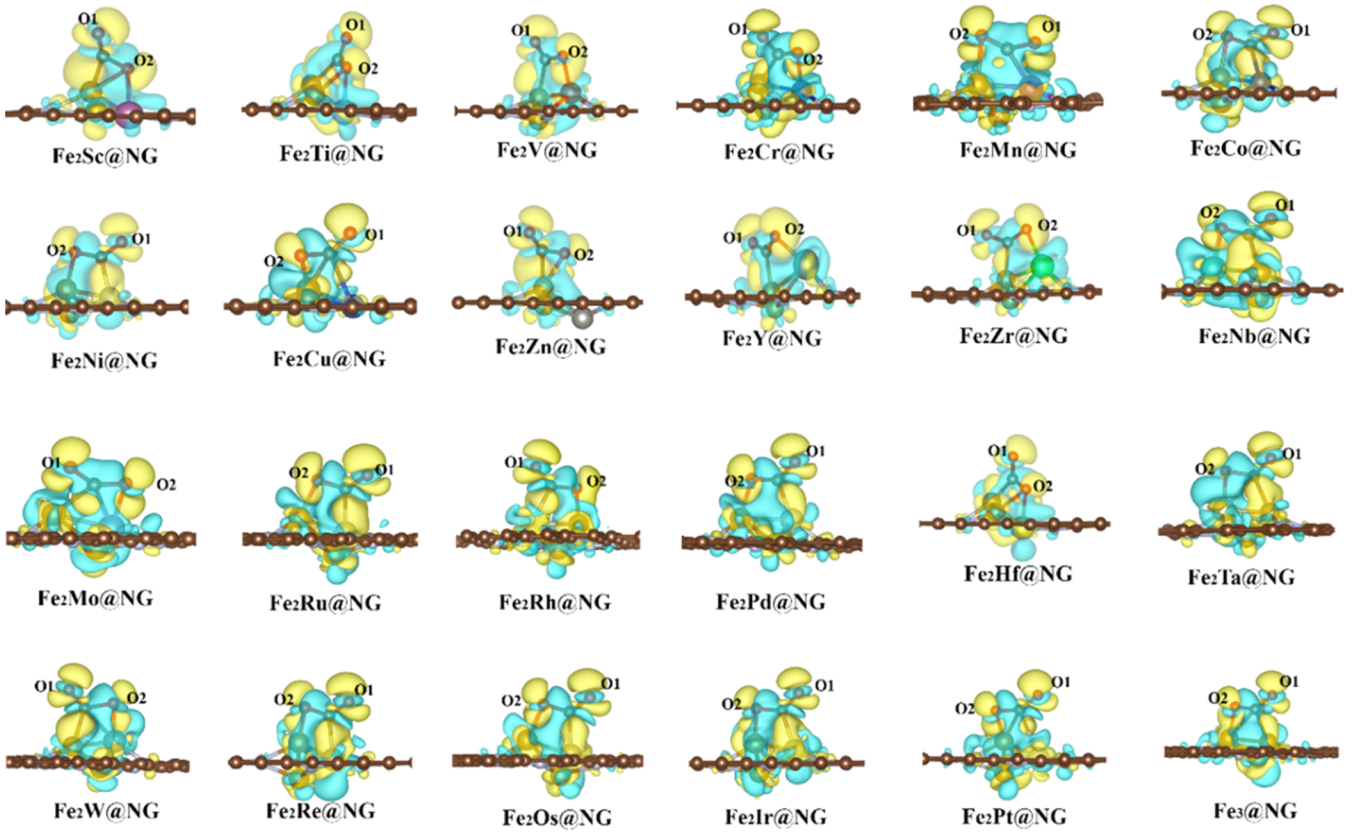

Figure 2. Differential charge diagram of CO_2-adsorbed Fe_2M@NG. The isosurface value was set as 0.002 e/Å^3. Yellow and cyan regions indicate electron accumulation and depletion, respectively.

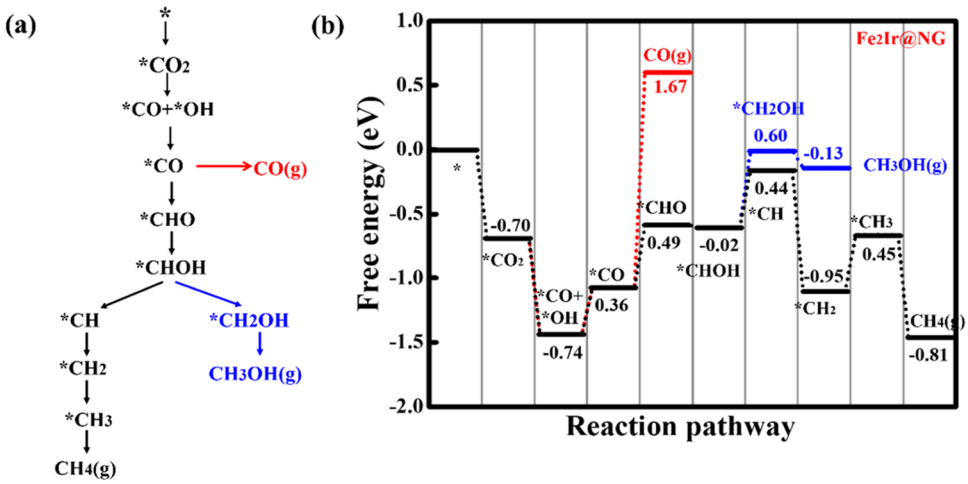

Figure 3. (a) Possible C_1 pathways of CO_2 reduction on the Fe_2Ir@NG, and (b) the corresponding free energy diagrams. Data denote the ΔG of each elementary step.

where E_{*CO_2}, E_*, and E_{CO_2} represent the energies of CO_2-adsorbed Fe_2M@NG, clean Fe_2M@NG, and a free CO_2 molecule, respectively. The E_{ad} values on these stable TACs ranged from −3.21 to −0.86 eV, and the adsorption energy of CO_2 on Fe_3@NG was calculated to be −1.57 eV, the same as the value reported in ref 17. The charge density difference of the CO_2-adsorbed Fe_2M@NG (Figure 2) showed that the electron depletion (cyan) is around bimetallic trimers, suggesting that the metal trimers donate electrons to the CO_2, and Bader charge analysis confirmed that the electrons are transferred from Fe_2M@NG to CO_2 by 0.57−0.98 e$^-$. The DOS (density of states, Figure S3) clearly shows the couplings between the *d* orbitals of the transition metal and the molecular orbitals of CO_2 near the Fermi level. The above results indicate that the TACs well activate the adsorbed CO_2, which is beneficial to facilitate CO_2 activation and reduction.

3.3. CO_2 Reduction Pathways. To find the optimal CO_2RR pathway, the free energies of the reaction over these TACs were calculated.[44] The reaction pathways of all catalysts are given in Table S3, and the ΔG of each elementary step is illustrated in free energy diagrams (Figures 3 and S4−S8). The CO_2 electroreduction reaction involves multiple electron

https://doi.org/10.1021/acsomega.2c01385
ACS Omega 2022, 7, 16080−16086

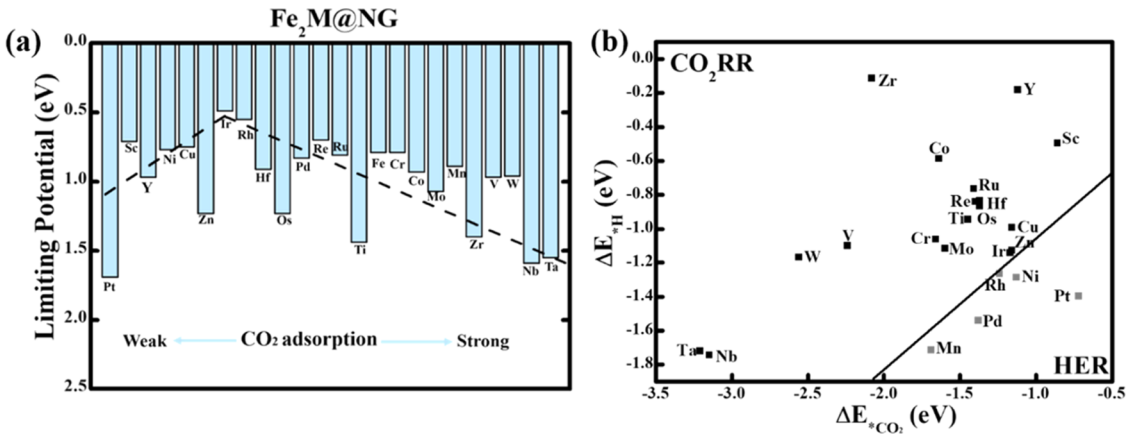

Figure 4. (a) Variation of limiting potentials of Fe_2M@NG catalysts for CO_2 reduction to C_1 products with respect to the CO_2 adsorption strength, and (b) comparison of the adsorption energies of $*CO_2$ and *H on Fe_2M@NG.

transfer paths, and the general form is $CO_2 + nH^+ + ne^- \rightarrow$ products + yH_2O.[45] In the formula, n is usually equal to 2, 4, and 8, and the corresponding products are CO/HCOOH, methanol, and methane.[46] The C_1 products and pathways are discussed in the following subsections, and the potential limiting steps (PLSs) and limiting potentials (η) of our examined TACs are illustrated in Table S4.

3.3.1. First Proton-Coupled Electron Transfer (PCET) Process. For n = 1, the first proton-coupled electron transfer (PCET) process involves the hydrogenation of the C or O atom.[47] We calculated the free energies of the first hydrogenation of $*CO_2$ in Figure S4. Therefore, the reaction pathway in this study was along * → *OCO → *H + *(O1/C/O2), *i.e.*, hydrogenation occurs at different positions (O1, C, O2 atoms). After structural optimization, we noticed that it is easier to form *OCOH on the five Fe_2M@NG (M = Co, Ni, Rh, Pd, Re), whose free energy changes are 0.16, 0.16, 0.44, −0.16, and 0.24 eV, respectively. *OCHO is favored to be generated over two Fe_2M@NG (M = Cr, Mn) with ΔG values of −0.44 and −0.34 eV, respectively. In addition, on the other 16 Fe_2M@NG (M = Sc, Ti, V, Cu, Zn, Y, Zr, Nb, Mo, Ru, Hf, Ta, W, Os, Ir, and Pt), protons preferentially react with O2 atom, thereby promoting breaking of the O1C−O2 bond. Therefore, compared with other products, the free energy for forming *CO + *OH on these TACs exhibits a downhill trend (−0.42, −1.15, −0.45, −1.12, −0.67, −0.55, −0.64, −0.85, −1.42, −0.90, −0.69, −0.81, −0.71, −0.72, −0.74, and −0.61 eV, respectively).

3.3.2. CO_2 Reduction to CO. After the first hydrogenation of $*CO_2$, the intermediates (*CO + *OH, *OCHO, and *OCOH) became the targets of the next proton−electron pair attack. Based on our computations, the following intermediates may be formed in the subsequent hydrogenation process: *COH + *OH (M = Sc), *CHO + *OH (M = Cr, Cu, W), *CO (after releasing a water molecule, M = Ti, V, Co, Ni, Zn, Y, Zr, Nb, Mo, Ru, Pd, Hf, Ta, Os, Ir, Pt), and *OCHOH (M = Mn, Rh, Re). The free energies of releasing the adsorbed CO were in the range of 0.92−2.62 eV; thus, the strong interaction between CO(g) and the TACs (Ti, V, Co, Ni, Zn, Y, Zr, Nb, Mo, Ru, Pd, Hf, Ta, Os, Ir, Pt) makes these TACs suffer CO poisoning; however, strong adsorption is beneficial to further hydrogenation of *CO on the other hand.

3.3.3. CO_2 Reduction to CH_3OH(g). Regarding the reduction of CO_2 to CH_3OH(g), we will continue the discussion based on the above results. For the third hydrogenation, the *COH + *OH intermediate on the Fe_2Sc@NG released a water molecule to form the *COH intermediate. The *CO species on the TACs may further form *COH (M = Ti, V, Zn, Y, Nb, Mo, Ru, Pd, Hf, Ta) or *CHO (M = Zr, Os, Ir, Pt). The *OCHOH on Fe_2M@NG (M = Mn, Rh, Re) may also be converted into *COH (M = Re) or *CHO species (M = Mn, Rh) by releasing an H_2O molecule. The *CHO + *OH species on Fe_2M@NG (M = Cr, Cu, W) were further reduced to *CHOH + *OH (M = Cu, W) and $*CH_2O$ + *OH (M = Cr). From the point of energy calculations, these hydroxyl intermediates will remain until the final hydrogenation into $*H_2O$. For the fourth hydrogenation, *CHOH (M = Sc, Ti, V, Zn, Y, Nb, Mo, Ru, Pd, Hf, Ta, Os, Ir, Pt), $*CH_3O$ + *OH (M = Cr), $*CH_2OH$ + *OH (M = Cu, W), and $*CH_2O$ (M = Mn, Zr, Rh, Re) will be formed on the Fe_2M@NG. Subsequently, these intermediates will be further reduced to $*CH_2OH$ (M = Sc, Ti, V, Zn, Y, Zr, Nb, Mo, Ru, Rh, Pd, Hf, Ta, Re, Os, Ir, Pt) and *OH (M = Cu, W, Cr) on Fe_2M@NG. For the final hydrogenation, $*CH_3OH$(g) (M = Sc, Ti, V, Zn, Y, Zr, Nb, Mo, Ru, Rh, Pd, Hf, Ta, Re, Os, Ir, Pt) and $*H_2O$ (M = Cu, W, Cr) will be formed. Moreover, the Fe_2M@NG (M = Cr, Cu, Rh, Pd, Ir) have small limiting potentials (0.76, 0.75, 0.55, 0.76, 0.60 V, respectively) in the pathway for CH_3OH formation. Their PLSs in the generation of CH_3OH(g) are *OH + $(H^+ + e^-) \rightarrow *H_2O$, (*CO + *OH) + $(H^+ + e^-) \rightarrow$ *CHO + *OH, *CHOH + $(H^+ + e^-) \rightarrow CH_2OH$, *COH + $(H^+ + e^-) \rightarrow$ *CHOH, and *CHOH + $(H^+ + e^-) \rightarrow *CH_2OH$, respectively. In comparison, the η to form CH_3OH(g) over the Fe_3@NG is 1.09 eV (PLS: *COH→ *CHOH, see Table S4 and Figure S8), largely because *COH is adsorbed on the hollow position of the Fe_3 cluster, making it unsuitable to attach H to C of *COH.

3.3.4. CO_2 Reduction to CH_4(g). The first few elementary steps are the same for the formation of CH_4(g) and CH_3OH(g); we thus mainly discuss the variant hydrogenating steps. For these Fe_2M@NG (M = Sc, Ti, V, Co, Ni, Zn, Y, Nb, Mo, Ru, Pd, Hf, Ta), the hydrogenation of *COH follows the pathway of *C → *CH → $*CH_2$ → $*CH_3$ → CH_4(g) to generate CH_4(g); the *CHO intermediates on the three Fe_2M@NG (M = Os, Ir, Pt) will be converted into CH_4(g) as follows, which is further hydrogenated to form *CH, and then follows the pathway: *CHO → *CHOH → *CH → $*CH_2$ → $*CH_3$ → CH_4(g). On the Fe_2Cr@NG and Fe_2W@NG, the pathways are $*CH_3O$ + *OH → *O + *OH+CH_4(g) → *OH +OH → *OH → $*H_2O$ and *CHOH + *OH → *CH + *OH

https://doi.org/10.1021/acsomega.2c01385
ACS Omega 2022, 7, 16080−16086

→ *CH_2+OH → *CH_3 + *OH → *OH → *H_2O, respectively. The three Fe_2M@NG (M = Sc, Ni, Ir) have small limiting potentials (0.71, 0.77, 0.49 V) in producing CH_4(g), and the PLSs are *CH_3 + (H^+ + e^-) → CH_4(g), *CO + (H^+ + e^-) → *COH, and *CHO + (H^+ + e^-) → *CHOH, respectively. Overall, for CO_2RR on the 23 bimetallic Fe_2M@NG catalysts, the Fe_2Ir@NG has the smallest limiting potential (η = 0.49 V) on the path toward CH_4 generation (* → *CO_2 → *CO + *OH → *CO → *CHO → *CHOH → *CH → *CH_2 → *CH_3 → CH_4(g)) among the three C_1 conversion routes (Figure 3), lower than the η value of the Fe_3@NG at the same level of theory (Figure S8, η = 0.79 V).

3.4. Essential Analysis of Catalytic Performance. Previous studies reveal that an ideal catalyst should provide moderate adsorption strength for all reactants, intermediates, and products.[48] Therefore, we evaluated the relationship between the limiting potential of the C_1 pathways over Fe_2M@NG and the CO_2 adsorption energy (Figure 4a). The results revealed that there is a volcanic relationship between the limiting potentials of the C_1 pathways and the CO_2 adsorption energies. By comparison, we found that six Fe_2M@NG have moderate E_{ad} for CO_2 (ranging from −1.40 to −1.13 eV) and have smaller η (0.77, 0.75, 0.55, 0.76, 0.70, and 0.49 V for Ni, Cu, Rh, Pd, Re, and Ir, respectively) compared with the Fe_3@NG (η = 0.79 V, E_{ad} = −1.57 eV). As the main competitive reaction of CO_2RR, the hydrogen evolution reaction (HER) also consumes proton−electron pairs (H^+ + e^-),[49] we considered the HER activity of the Fe_2M@NG. We first calculated the E_{ad} of *H on Fe_2M@NG and compared with the E_{ad} of *CO_2 (Figure 4b) and found that on the Fe_2M@NG (M = Rh, Ni, Pd, Mn, Pt), whose η values are lower than 0.79 V of Fe_3@NG, the E_{ad} of *H is more negative than that of CO_2, indicating that it is not conducive for the progress of CO_2RR on these TACs.[17] However, the Fe_2Ir@NG has a stronger interaction with *CO_2 than *H, and the ΔG (0.94 eV) for the HER (Figure S9) is much greater than the maximum ΔG for CO_2RR toward CH_4(g) (0.49 eV). Thus, the Fe_2Ir@NG has high selectivity for CO_2RR.

According to the density of states (Figure S3), compared to the case of Fe_3@NG, in bimetallic TACs, the coupling between M and Fe_2 weakens or strengthens the hybridization with CO_2 near the Fermi level and thereby modulates the catalytic capability of the TACs. Among the 23 bimetallic TACs, the Fe_2Ir@NG has a medium adsorption strength for CO_2 and a minimum limiting potential and can effectively suppress the HER. All in all, the Fe_2Ir@NG is a very promising catalyst for CO_2 reduction to CH_4.

4. CONCLUSIONS

In summary, by performing comprehensive first-principles calculations, we explored the stability and catalytic behavior of 23 bimetallic triple-atom catalysts (Fe_2M@NG) for CO_2 reduction to C_1 products (including CO, CH_3OH, and CH_4). Our results showed that the supported bimetallic trimers provide sufficient adsorption sites to adsorb CO_2, thereby effectively activating the CO_2 and promoting the breaking of the C−O bond. The synergy between Ir and Fe atoms in the outstanding TAC of Fe_2Ir@NG improves the catalytic activity (low limiting potential 0.49 V for CH_4 formation) and selectivity (reluctant for the competing reaction HER) for CO_2RR. Our theoretical study offers guidance to design bimetallic TACs with high catalytic performance beyond CO_2RR.

ASSOCIATED CONTENT

Supporting Information

The Supporting Information is available free of charge at https://pubs.acs.org/doi/10.1021/acsomega.2c01385.

The $G(T)$ of the free gas molecules and adsorbed intermediates on Fe_2M@NG; the binding energy of M, bond lengths, and the adsorption energy of CO_2 for the Fe_2M@NG; the potential limiting steps of CO_2RR via C1 pathways and the limiting potentials on Fe_2M@N; top and side views of optimized Fe_2M@NG structures; the energy profile and the final structure of FPMD simulation of Fe_2Zn@NG at 500 K; the density of states of the CO_2-adsorbed Fe_2M@NG; the free energy diagram of the first hydrogenation of *CO_2; the free energy diagrams of different pathways on Fe_2M@NG and Fe_3@NG; the free energy diagram of the HER on Fe_2Ir@NG (PDF)

AUTHOR INFORMATION

Corresponding Author

Fengyu Li − *School of Physical Science and Technology, Inner Mongolia University, Hohhot 010021, China;* orcid.org/0000-0002-9483-8554; Email: fengyuli@imu.edu.cn

Authors

Bing Han − *School of Physical Science and Technology, Inner Mongolia University, Hohhot 010021, China*

Haihong Meng − *School of Physical Science and Technology, Inner Mongolia University, Hohhot 010021, China*

Complete contact information is available at: https://pubs.acs.org/10.1021/acsomega.2c01385

Notes

The authors declare no competing financial interest.

ACKNOWLEDGMENTS

This work was supported by the National Natural Science Foundation of China (11704203, 11964024), the "Grassland Talents" project of Inner Mongolia autonomous region (12000-12102613), the young science and technology talents cultivation project (21221505) and the special funding for postgraduate innovation and entrepreneurship of Inner Mongolia University (11200-121024). The authors thank the computational support from Beijing PARATERA. The authors are grateful to Wei Pei at Dalian University of Technology for constructive discussions.

REFERENCES

(1) Saeidi, S.; Amin, N. A. S.; Rahimpour, M. R. Hydrogenation of CO_2 to value-added products—a review and potential future developments. *J. CO2 Util.* **2014**, *5*, 66−81.

(2) Liu, J.; Chen, C.; Zhang, K.; Zhang, L. Applications of metal−organic framework composites in CO_2 capture and conversion. *Chin. Chem. Lett.* **2021**, *32*, 649−659.

(3) Wang, S.; Li, L.; Li, J.; Yuan, C.; Kang, Y.; Hui, K. S.; Zhang, J.; Bin, F.; Fan, X.; Chen, F.; Hui, K. N. High-throughput screening of nitrogen-coordinated bimetal catalysts for multielectron reduction of CO_2 to CH_4 with high selectivity and low limiting potential. *J. Phys. Chem. C* **2021**, *125*, 7155−7165.

(4) Alotto, P.; Guarnierin, M.; Moro, F. Redox flow batteries for the storage of renewable energy: a review. *Renewable Sustainable Energy Rev.* **2014**, *29*, 325−335.

(5) Peng, C.-J.; Wu, X.-T.; Zeng, G.; Zhu, Q.-L. In situ bismuth nanosheet assembly for highly selective electrocatalytic CO_2 reduction to formate. *Chem. Asian J.* **2021**, *16*, 1539−1544.
(6) Zhang, H.; Xu, H.; Li, Y.; Pan, X.; Li, L. Nanocable catalysts MTe (M = Pt, PtCu)@UIO-67 for CO_2 conversion. *Sci. China Mater.* **2020**, *63*, 769−778.
(7) Du, Y.; An, W. Effects of uniaxial lattice strain and explicit water solvation on CO_2 electroreduction over a Cu electrode: a density functional theory perspective. *J. Phys. Chem. C* **2021**, *125*, 9138−9149.
(8) Zhang, J.; Wang, Y.; Wang, H.; Zhong, D.; Lu, T. Enhancing photocatalytic performance of metal-organic frameworks for CO_2 reduction by a bimetallic strategy. *Chin. Chem. Lett.* **2022**, *33*, 2065−2068.
(9) Sun, K.; Zhang, Z.; Shen, C.; Rui, N.; Liu, C.-J. The feasibility study of the indium oxide supported silver catalyst for selective hydrogenation of CO_2 to methanol. *Green Energy Environ.* **2021**, DOI: 10.1016/j.gee.2021.05.004.
(10) Liang, X.; Ren, X.; Guo, M.; Li, Y.; Xiong, W.; Guan, W.; Gao, L.; Liu, A. CO_2 electroreduction by AuCu bimetallic clusters: a first principles study. *Int. J. Energy Res.* **2021**, *45*, 18684−18694.
(11) Liu, T.; Wang, G.; Bao, X. Electrochemical CO_2 reduction reaction on 3d transition metal single-atom catalysts supported on graphdiyne: a DFT study. *J. Phys. Chem. C* **2021**, *125*, 26013−26020.
(12) Gong, J.; English, N. J.; Pant, D.; Patzke, G. R.; Protti, S.; Zhang, T. Power-to-X: lighting the path to a net-zero-emission future. *ACS Sustainable Chem. Eng.* **2021**, *9*, 7179−7181.
(13) Hori, Y.; Wakebe, H.; Tsukamoto, T.; Koga, O. Electrocatalytic process of CO selectivity in electrochemical reduction of CO_2 at metal electrodes in aqueous media. *Electrochim. Acta* **1994**, *39*, 1833−1839.
(14) Guo, C.; Zhang, T.; Lu, X.; Wu, C. L. Rational design and effective control of gold-based bimetallic electrocatalyst for boosting CO_2 reduction reaction: a first-principles study. *ChemSusChem* **2021**, *14*, 2731−2739.
(15) Ju, W.; Bagger, A.; Hao, G.-P.; Varela, A. S.; Sinev, I.; Bon, V.; Cuenya, B. R.; Kaskel, S.; Rossmeisl, J.; Strasser, P. Understanding activity and selectivity of metal-nitrogen-doped carbon catalysts for electrochemical reduction of CO_2. *Nat. Commun.* **2017**, *8*, No. 944.
(16) Cometto, C.; Ugolotti, A.; Grazietti, E.; Moretto, A.; Bottaro, G.; Armelao, L.; Valentin, C. D.; Calvillo, L.; Granozzi, G. Copper single-atoms embedded in 2D graphitic carbon nitride for the CO_2 reduction. *NPJ 2D Mater. Appl* **2021**, *5*, No. 63.
(17) Pei, W.; Zhou, S.; Zhao, J.; Xu, X.; Du, Y.; Dou, S. X. Immobilized trimeric metal clusters: A family of the smallest catalysts for selective CO_2 reduction toward multi-carbon products. *Nano Energy* **2020**, *76*, No. 105049.
(18) Gao, Z.; Li, J.; Zhang, Z.; Hu, W. Recent advances in carbon-based materials for electrochemical CO_2 reduction reaction. *Chin. Chem. Lett.* **2021**, DOI: 10.1016/j.cclet.2021.09.037.
(19) Han, J.; Deng, X.; Chen, K.; Imhanria, S.; Sun, Y.; Wang, W. Electrochemical conversion of CO_2 into tunable syngas on a B, P, N tri-doped carbon. *Renewable Energy* **2021**, *177*, 636−642.
(20) Yang, Q.; Yang, C. C.; Lin, C.-H.; Jiang, H.-L. Metal−organic-framework-derived hollow N-doped porous carbon with ultrahigh concentrations of single Zn atoms for efficient carbon dioxide conversion. *Angew. Chem., Int. Ed.* **2019**, *58*, 3511−3515.
(21) Zhang, X.; Guo, J.; Guan, P.; Liu, C.; Huang, H.; Xue, F.; Dong, X.; Pennycook, S. J.; Chisholm, M. F. Catalytically active single-atom niobium in graphitic layers. *Nat. Commun.* **2013**, *4*, No. 1924.
(22) Sun, J.-F.; Xu, Q.-Q.; Qi, J.-L.; Zhou, D.; Zhu, H.-Y.; Yin, J.-Z. Isolated single atoms anchored on N-doped carbon materials as a highly efficient catalyst for electrochemical and organic reactions. *ACS Sustainable Chem. Eng.* **2020**, *8*, 14630−14656.
(23) Rasheed, T.; Shafi, S.; Anwar, M. T.; Rizwan, K.; Ahmad, T.; Bilal, M. Revisiting photo and electro-catalytic modalities for sustainable conversion of CO_2. *Appl. Catal., A* **2021**, *623*, No. 118248.
(24) Yang, X.-F.; Wang, A.; Qiao, B.; Li, J.; Liu, J.; Zhang, T. Single-atom catalysts: a new frontier in heterogeneous catalysis. *Acc. Chem. Res.* **2013**, *46*, 1740−1748.
(25) Feng, Z.; Tang, Y.; Ma, Y.; Li, Y.; Dai, Y.; Ding, H.; Su, G.; Dai, X. Theoretical investigation of CO_2 electroreduction on N (B)-doped graphdiyne mononlayer supported single copper atom. *Appl. Surf. Sci.* **2021**, *538*, No. 148145.
(26) Huo, S.; Lu, J.; Wang, X. Recent progress in electrochemical reduction of carbon dioxide on metal single- atom catalysts. *Energy Sci. Eng.* **2021**, DOI: 10.1002/ese3.1036.
(27) Pan, Y.; Zhang, C.; Liu, Z.; Chen, C.; Li, Y. Structural regulation with atomic-level precision: from single-atomic site to diatomic and atomic interface catalysis. *Matter* **2020**, *2*, 78−110.
(28) Zhang, J.; Huang, Q.; Wang, J.; Wang, J.; Zhang, J.; Zhao, Y. Supported dual-atom catalysts: Preparation, characterization, and potential applications. *Chin. J. Catal.* **2020**, *41*, 783−798.
(29) Liu, H.; Huang, Q.; An, W.; Wang, Y.; Men, Y.; Liu, S. Dual-atom active sites embedded in two-dimensional C_2N for efficient CO_2 electroreduction: A computational study. *J. Energy Chem.* **2021**, *61*, 507−516.
(30) Chen, Z. W.; Chen, L. X.; Yang, C. C.; Jiang, Q. Atomic (single, double, and triple atoms) catalysis: frontiers, opportunities, and challenges. *J. Mater. Chem. A* **2019**, *7*, 3492−3515.
(31) Han, B.; Meng, H.; Li, F.; Zhao, J. Fe_3 cluster anchored on the C_2N monolayer for efficient electrochemical nitrogen fixation. *Catalysts* **2020**, *10*, 974.
(32) Ji, S.; Chen, Y.; Fu, Q.; Chen, Y.; Dong, J.; Chen, W.; Li, Z.; Wang, Y.; Gu, L.; He, W.; Chen, C.; Peng, Q.; Huang, Y.; Duan, X.; Wang, D.; Draxl, C.; Li, Y. Confined pyrolysis within metal−organic frameworks to form uniform Ru_3 clusters for efficient oxidation of alcohols. *J. Am. Chem. Soc.* **2017**, *139*, 9795−9798.
(33) Zhang, J.; Deng, Y.; Cai, X.; Chen, Y.; Peng, M.; Jia, Z.; Jiang, Z.; Ren, P.; Yao, S.; Xie, J.; Xiao, D.; Wen, X.; Wang, N.; Liu, H.; Ma, D. Tin-assisted fully exposed platinum clusters stabilized on defect-rich graphene for dehydrogenation reaction. *ACS Catal.* **2019**, *9*, 5998−6005.
(34) Kresse, G.; Furthmüller, F. Efficient iterative schemes for ab initio total-energy calculations using a plane-wave basis set. *Phys. Rev. B* **1996**, *54*, 11169−11186.
(35) Perdew, J. P.; Burke, K.; Ernzerhof, M. Generalized gradient approximation made simple. *Phys. Rev. Lett.* **1996**, *77*, 3865−3868.
(36) Grimme, S.; Antony, J.; Ehrlich, S.; Krieg, H. A consistent and accurate ab initio parametrization of density functional dispersion correction (DFT-D) for the 94 elements H-Pu. *J. Chem. Phys.* **2010**, *132*, No. 154104.
(37) Monkhorst, H. J.; Pack, D. J. Special points for Brillouin-zone integrations. *Phys. Rev. B* **1976**, *13*, 5188−5192.
(38) Nørskov, J. K.; Rossmeisl, J.; Logadottir, A.; Lindqvist, L.; Kitchin, J. R.; Bligaard, T.; Jonsson, H. Origin of the overpotential for oxygen reduction at a fuel-cell cathode. *J. Phys. Chem. B* **2004**, *108*, 17886−17892.
(39) Tian, Y.; Wang, Y.; Yan, L.; Zhao, J.; Su, Z. Electrochemical reduction of carbon dioxide on the two−dimensional M_3(Hexaiminotriphenylene)$_2$ sheet: a computational study. *Appl. Surf. Sci.* **2019**, *467−468*, 98−103.
(40) Chen, H.; Handoko, A. D.; Xiao, J.; Feng, X.; Fan, Y.; Wang, T.; Legut, D.; Seh, Z. W.; Zhang, Q. Catalytic effect on CO_2 electroreduction by hydroxyl-terminated two-dimensional MXenes. *ACS Appl. Mater. Interfaces* **2019**, *11*, 36571−36579.
(41) Wang, X.; Niu, H.; Liu, Y.; Shao, C.; Robertson, J.; Zhang, Z.; Guo, Y. Theoretical investigation on graphene-supported single-atom catalysts for electrochemical CO_2 reduction. *Catal. Sci. Technol.* **2020**, *10*, 8465−8472.
(42) Skúlason, E.; Bligaard, T.; Gudmundsdottir, S.; Studt, F.; Rossmeisl, J.; Abild-Pedersen, F.; Vegge, T.; Jonsson, H.; Norskov, J. K. A theoretical evaluation of possible transition metal electro-catalysts for N_2 reduction. *Phys. Chem. Chem. Phys.* **2012**, *14*, 1235−1245.

https://doi.org/10.1021/acsomega.2c01385
ACS Omega 2022, 7, 16080−16086

(43) Liu, T.; Wang, Q.; Wang, G.; Bao, X. Electrochemical CO_2 reduction on graphdiyne: a DFT study. *Green Chem.* **2021**, *23*, 1212−1219.
(44) Yuan, H.; Li, Z.; Zeng, X. C.; Yang, J. Descriptor-based design principle for two-dimensional single-atom catalysts: carbon dioxide electroreduction. *J. Phys. Chem. Lett.* **2020**, *11*, 3481−3487.
(45) Zong, X.; Jin, Y.; Liu, C.; Yao, Y.; Zhang, J.; Luo, W.; Züttel, A.; Xiong, Y. Electrospun nanofibers for electrochemical reduction of CO_2: a mini review. *Electrochem. Commun.* **2021**, *124*, No. 106968.
(46) Zou, Y.; Wang, S. An investigation of active sites for electrochemical CO_2 reduction reactions: from in situ characterization to rational design. *Adv. Sci.* **2021**, *8*, No. 2003579.
(47) Huang, L.; Li, W.; Zeng, M.; He, G.; Shearing, P. R.; Parkin, I. P.; Brett, D. J. L. Metal-nitrogen-doped carbon single-atom electrocatalysts for CO_2 electroreduction. *Composites, Part B* **2021**, *220*, No. 108986.
(48) Zeng, H.; Liu, X.; Chen, F.; Chen, Z.; Fan, X.; Lau, W. Single atoms on a nitrogen-doped boron Phosphide monolayer: a new promising bifunctional electrocatalyst for ORR and OER. *ACS Appl. Mater. Interfaces* **2020**, *12*, 52549−52559.
(49) Liu, S.; Cheng, L.; Li, K.; Yin, C.; Tang, H.; Wang, Y.; Wu, Z. RuN_4 doped graphene oxide, a highly efficient bifunctional catalyst for oxygen reduction and CO_2 reduction from computational study. *ACS Sustainable Chem. Eng.* **2019**, *7*, 8136−8144.

https://doi.org/10.1021/acsomega.2c01385
ACS Omega 2022, 7, 16080−16086